

# On the initiation and evolution of dielectric breakdown in auto-magnetizing liner experiments

G. A. Shipley,<sup>1,a)</sup> T. J. Awe,<sup>1</sup> B. T. Hutsel,<sup>1</sup> and D. A. Yager-Elorriaga<sup>1</sup>

<sup>1</sup>Sandia National Laboratories, Albuquerque, New Mexico 87185, USA

<sup>a)</sup>Author to whom correspondence should be addressed: [gashipl@sandia.gov](mailto:gashipl@sandia.gov)

AutoMag liners are cylindrical tubes composed of discrete metallic helices encapsulated in insulating material; when driven with a  $\sim 2$  MA,  $\sim 100$  ns prepulse on the 20 MA, 100-ns rise time Z accelerator, AutoMag targets produced  $>150$  T internal axial magnetic fields [G. A. Shipley et al., Phys. Plasmas 26, 052705 (2019)]. Once the current rise rate of the pulsed power driver reaches sufficient magnitude, the induced electric fields in the liner cause dielectric breakdown of the insulator material and, with sufficient current, the cylindrical target radially implodes. The dielectric breakdown process of the insulating material in auto-magnetizing (AutoMag) liners has been studied in experiments on the 500-900 kA,  $\sim 100$ -ns rise time Mykonos accelerator. Multi-frame gated imaging enabled the first time resolved observations of photoemission from dynamically evolving plasma distributions during the breakdown process in AutoMag targets. Using magnetohydrodynamic simulations, we calculate the induced electric field distribution and provide detailed comparison to the experimental data. We find that breakdown in AutoMag targets does not primarily depend on the induced electric field in the gaps between conductive helices as previously thought. Finally, to better control the dielectric breakdown time, a 12-32 mJ, 170 ps ultraviolet ( $\lambda = 266$  nm) laser was implemented to irradiate the outer surface of AutoMag targets to promote breakdown in a controlled manner at lower internal axial field. The laser had an observable effect on the time of breakdown and subsequent plasma evolution, indicating that pulsed UV lasers can be used to control breakdown timing in AutoMag.

## I. Introduction

Magnetized Liner Inertial Fusion (MagLIF<sup>1,2</sup>) is a magneto-inertial fusion approach that uses a pulsed current to magnetically compress a cylindrical volume of axially premagnetized, laser-preheated fusion fuel. In MagLIF, pre-seeded, axially-oriented magnetic fields,  $B_{z,0}$ , in the 10-20 T range are flux compressed to O(kT) to mitigate electron thermal conduction losses from the fusion fuel radially outward to the liner during  $\sim 100$  ns implosions on the Z accelerator<sup>3,4</sup> while introducing the trapping of charged fusion particles during thermonuclear burn. Such fields are provided by external magnetic field coils<sup>5</sup>. For  $B_{z,0} > 15$  T, external coil systems limit diagnostic access to the imploding target. Additionally, the present coils are limited to  $<30$  T premagnetization fields. Calculations<sup>1</sup> indicate that higher fields may enable higher neutron yields via improvement of thermal insulation of the fuel.

Auto-magnetizing (AutoMag) liners<sup>6</sup> are designed to supplant external field coils and facilitate magnetization of a cm-scale cylindrical volume to the 30-100 T level on  $\sim 100$ -ns timescales prior to radial implosion of the target. AutoMag liners first magnetize the internal cylindrical volume by flowing helical current sourced by the pulsed power driver through discrete helical conductors encapsulated by electrically insulating material (Fig. 1(a) and 1(b)). Beryllium ( $\rho_{Be}=1.85$  g/cm<sup>3</sup>) and aluminum ( $\rho_{Al}=2.7$  g/cm<sup>3</sup>) have been used for the conductive material while flowable epoxies Stycast and EPON ( $\rho_{Stycast} \cong \rho_{EPON} \cong 1.1$  g/cm<sup>3</sup>) have been used for the insulating encapsulant, resulting in helically oriented, macroscopic nonuniformities in the liner mass density. Initially, the driver current rise rate,  $dI/dt$ , is kept low enough to prevent induced electric fields in the target (proportional to  $dI/dt$ ) from causing dielectric breakdown of the insulating material. When the driver current rise rate increases beyond a certain threshold, the insulating material undergoes dielectric breakdown,

the current reorients from helical to primarily axial, and the internal axial magnetic field production ceases. Although internal field production was expected to cease when breakdown occurs due to complete reorientation of helical current to axial current, experiments<sup>7</sup> on the Z facility revealed that the measured internal axial magnetic field continued to rise after breakdown initiation, though at a reduced rate than prior to breakdown, indicating that some helical current persisted in the target. This persistent helical current and continued field production resulted in the production of >150 T uncompressed internal axial magnetic fields,  $B_{z,in}$  (measured by miniature magnetic field probes<sup>9</sup> called “microBdots”). As the drive current continues to increase, the cylindrical z-pinch target is radially imploded and  $B_{z,in}$  is expected to compress to O(kT) without significant magnetic flux losses due to resistive diffusion on the ~100-ns timescale of the implosion.

AutoMag liners have consistently produced 20-90 T internal axial magnetic fields during experiments<sup>8</sup> on the 500-900 kA, ~100 ns rise time Mykonos accelerator<sup>10</sup> (Fig. 1(c) and 1(d)). AutoMag liner have also demonstrated encouraging levels of cylindrical implosion stability (despite the initial macroscopic, helically oriented nonuniformities in mass density and electrical conductivity inherent to the target design) during experiments<sup>7</sup> on Z. AutoMag liners eliminate the need for the external field coils entirely, enabling unimpeded diagnostic access to the imploding target. The first series of experiments<sup>8</sup> on Mykonos confirmed that strong magnetic fields can be produced inside of AutoMag liners and indicated that breakdown occurs as a function of the average induced electric field within the helical gaps at the axial midplane of the target,  $E_{gap}$ , and insulator configuration. However, the unexpected rise in  $B_{z,in}$  after breakdown initiation during Z experiments produced questions regarding the details of the initiation and evolution of breakdown. One such question is how strong of an indicator the calculated  $E_{gap}$  is for determining the time at which AutoMag targets would undergo breakdown.

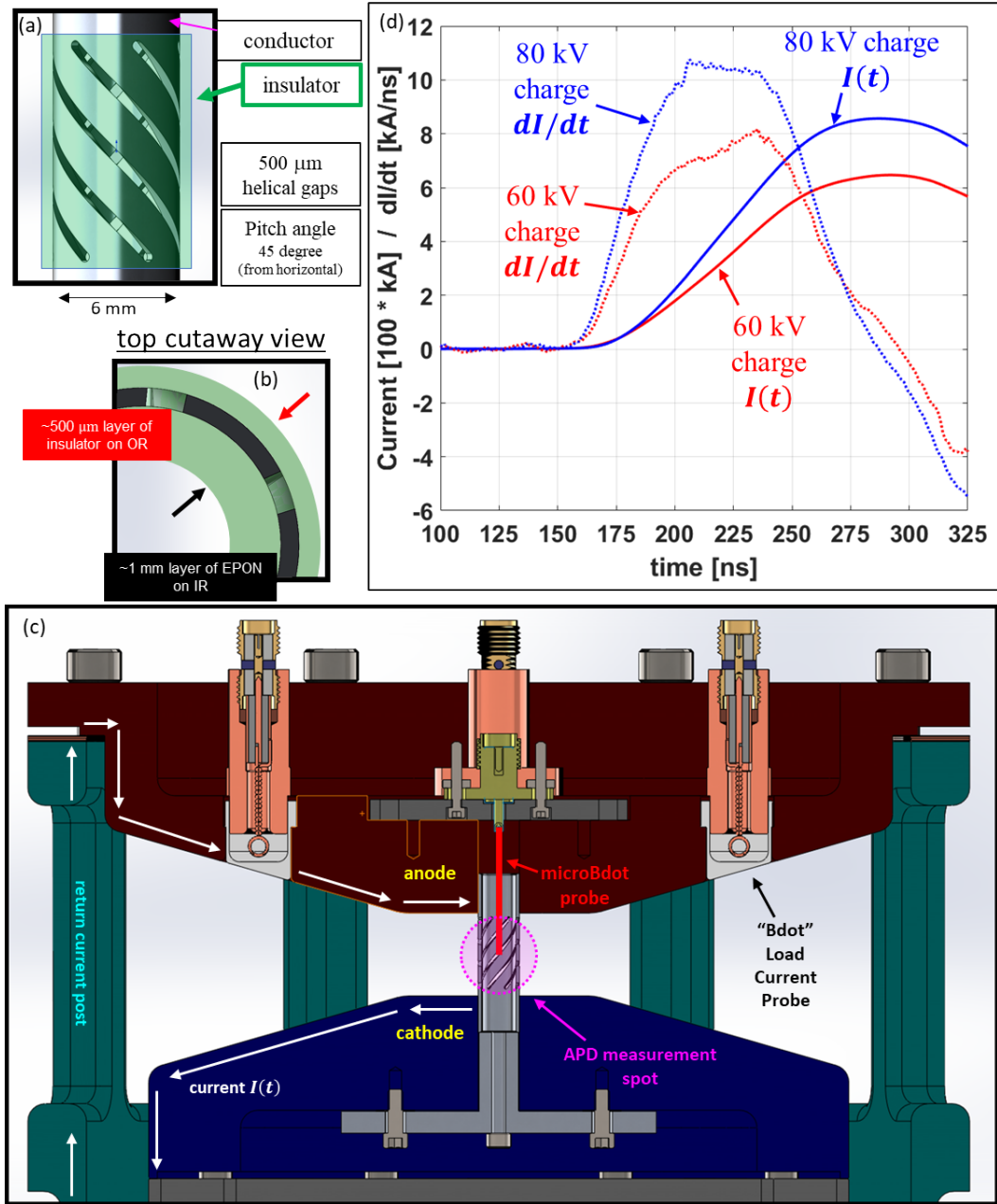


FIG. 1. – (a) A side schematic view of an AutoMag target shows the basic target dimensions and the configuration of conductive and insulating material. (b) A top schematic view of an AutoMag target shows the thickness of encapsulating insulating material in AutoMag targets fielded in experiments on the Mykonos accelerator. (c) A cutaway view of the target hardware fielded in experiments on the Mykonos accelerator shows (schematically) the direction of current flow (white arrows), the anode (red), the cathode (blue), the view of the DET10A silicon photodiode and APD430A avalanche photodiode detectors (magenta), the location of the microBdot probes inside of the target (red), and the location of the current monitor “Bdot” probe in the anode side of the end of the pulsed power transmission line. (d) A plot of drive current in solid color and current rise rate in dotted color for the two machine configurations used in experiments reported in this article: 60 kV charge voltage in red and 80 kV charge voltage in blue.

Controlling the internal axial magnetic field in AutoMag for use in MagLIF requires a more detailed understanding of the initiation and evolution of the dielectric breakdown process for this type of target. Ideally, internal field production in AutoMag liners would cease at a level that is optimal for the application of interest (e.g.,  $B_{z,in} = 30\text{-}50\text{ T}$  for MagLIF<sup>11</sup>); for MagLIF, magnetic fields inside of

the target above the optimal range could reduce the compressional work done on the fusion fuel during the implosion as the magnetic energy of the field begins to dominate the thermal energy of the preheated fuel. Previous experimental work<sup>8</sup> suggested that the induced electric fields in the target influence breakdown initiation and evolution, but due to the absence of time resolved imaging, assessments of the factors influencing breakdown in AutoMag have been limited. In Section II, we present time resolved imaging data of the breakdown process in AutoMag targets fielded on the Mykonos accelerator and discuss our hypotheses regarding factors contributing to the initiation time and the subsequent evolution of breakdown. In Section III, we discuss the use of a pulsed UV laser to control breakdown initiation. In Section IV, we briefly summarize results from AutoMag experiments and compare results from experiments on Mykonos and Z. In Section V, we discuss the use of a new insulating material in AutoMag targets composed of a mixture of flowable epoxy and volumetrically distributed (semi-conductive) boron carbide powder; this mixture was explored to determine whether an insulator with a mass density matching beryllium (an ideal material for MagLIF experiments on Z) would result in diagnosable differences in field production and breakdown. Finally, in Section VI, we provide concluding remarks and consider future directions for research on the AutoMag target concept.

## **II. Study of Dielectric Breakdown Evolution**

A 12-frame gated imager was fielded using 5-ns frame widths and no inter-frame delay during Mykonos experiments to assess the evolution of the dielectric breakdown process in AutoMag liners (Fig. 2). Informed by previous experimental results<sup>8</sup>, targets were designed to repeatably and reliably undergo dielectric breakdown; this was primarily accomplished by using targets with more shallowly pitched helices, particularly 20° helices, and by increasing the peak current of the pulsed power driver to access larger  $dI/dt$  (and thus larger induced electric fields in/across the targets). In previous experiments, it was clear that both the pitch of the conductive helices and the magnitude of  $dI/dt$  contribute to the propensity for breakdown. In accordance with Faraday's Law, more shallowly pitched helices produce stronger, time-varying internal axial magnetic fields per unit drive current which induce stronger electric fields in the target. Similarly, for a given helical pitch angle, higher driver current rise rates induce stronger electric fields.

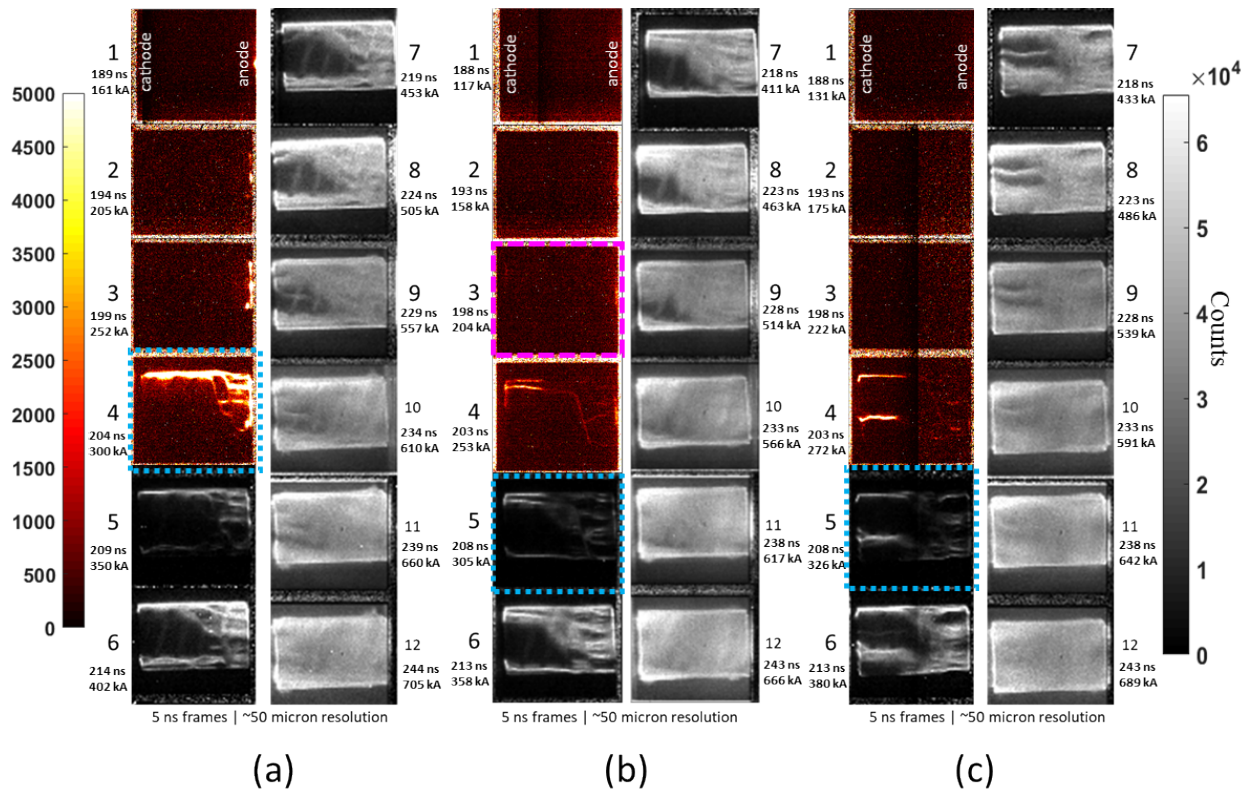


FIG. 2. – (a), (b), and (c) are each 12-frame imager datasets from AutoMag experiments that used targets with  $20^\circ$  metallic helices and helical gaps that were 500- $\mu\text{m}$  wide. All three datasets are from experiments that had a  $\sim 850$  kA peak current pulse (see Fig. 1(d)). In all images, the cathode is on the left and the anode is on the right. For all three experiments, the breakdown evolution occurred very similarly, particularly with respect to the formation of discrete emitting filaments on the outer surface of the insulating material which then gave way to quasi-uniform emitting distributions. Earlier frames have an enhanced data scale (shown on the left side of the plot) to demonstrate the relative brightness of the earliest emitting filaments to form in the breakdown process compared to the 1000-2000 count noise level of the imager diagnostic. The data scale colormap with the wider range reflecting the overall higher brightness of later frames is shown on the right side of the plot. Light blue dotted boxes indicate the frames during which breakdown initiation was inferred from APD data and the magenta dashed box in (b) indicates the frame during which breakdown initiation was inferred from microBdot data. MicroBdot data were not captured for (a) and (c).

For experiments reported here, the timing of initiation of dielectric breakdown was assessed with (1) an APD430A (avalanche photodiode) which measured visible photoemission from the target and (2) with microBdots installed on axis inside of the target. A less sensitive DET10A silicon photodiode enabled assessment of the time resolved photoemission that occurs after breakdown initiation. The sensitive avalanche diode measured the earliest emission from breakdown initiation, but importantly, was filtered using broadband, visible spectrum neutral density filters so as not to register significant signal when irradiated by photoemission from the electrode contacts. In addition, the APD430 was configured so that the electrode contacts overlapped minimally with the circular field of view (Fig. 1(c)), minimizing their contribution to the measurement. In experiments where multi-frame imaging and microBdot data confirm that breakdown *has not* occurred, the avalanche diode does not “turn on.” This provides a consistent method to distinguish between breakdown emission and electrode contact emission across multiple experiments. We postulate that electrode contact emission could be reduced or eliminated by improving electrode current contacts, perhaps through penetrative contact between the target and the electrode materials (i.e., “knife edge” contacts), use of soft metal contacts<sup>12</sup>, or through brazing/welding of the target to the electrodes. Any of these techniques (or a combination) could aid in reducing contact resistance and eliminating

vacuum gaps between the target and electrode surfaces that can give rise to arcing, though we note that experiments to date indicate that such localized arcing does not appear to be a significant factor in driving global breakdown in AutoMag experiments. As in previous Mykonos experiments, the integrated signal from the microBdot probes maintains direct proportionality with driver current prior to breakdown ( $B_{z,in}(t) = \alpha I(t)$ , where  $\alpha$  is a constant of proportionality only valid prior to breakdown), so departure from that scaling indicates breakdown initiation.

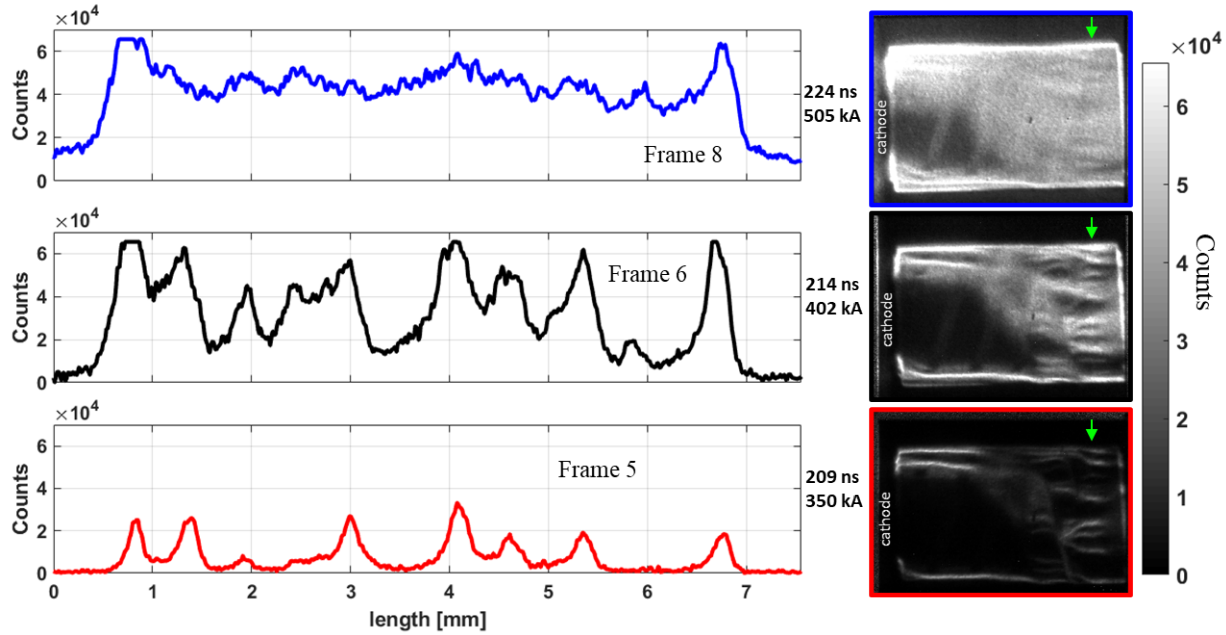


FIG. 3. - Visible spectrum images taken using the 12-frame gated imager diagnostic. These frames (shown at the right) are taken from the same experiment as Fig. 2(b). Lineouts of photoemission were taken through the section of the image indicated by green arrows in each image. The lineouts were vertical with respect to the orientation of the images in the right of the figure.

The emission distributions captured by the multi-frame imager, shown in Fig. 3, indicate a surface flashover phenomenon, rather than a bulk breakdown process occurring beneath the insulator surface, which evolves as follows: (1) discrete, emitting filaments form on the insulator surface, apparently originating from both the cathode and anode sides of the target; (2) additional emitting filaments appear within 5-10 ns after the first filaments; (3) the spaces between discrete emitting filaments begin to emit; (4) the emitting distribution becomes quasi-uniform as the inter-filament spaces begin emitting more brightly with time and eventually emit as brightly as the discrete filaments. Importantly, although the multi-frame imager captures emission indicative of a surface flashover phenomenon (a particular type of dielectric breakdown), the diagnostics fielded in these experiments cannot definitively determine that other breakdown/flashover processes (such as breakdown within the bulk volume of the insulator or a surface flashover on the inner surface of the insulator) are not occurring concurrently with the outer surface flashover process observed. The observed breakdown process takes approximately 30-35 ns from the time of formation of the earliest emitting filaments to the time at which the distribution appears to be emitting quasi-uniformly from the outer liner surface based on analysis of 12-frame imaging data captured during 80 kV charge, 500- $\mu\text{m}$  gap, 20 $^\circ$  AutoMag targets (such as those shown in Fig. 2). In other words, the observed breakdown process elapses during the extent of 6 to 7 frames captured by the multi-frame imager.

The structure of the individual, early-time emitting filaments changes with time, resulting in the quasi-uniform emission distribution seen in later frames (Fig. 3). The earliest emitting filaments have

a range of full-width-half-maximum (FWHM) widths of 160-200  $\mu\text{m}$  (Fig. 3, bottom). By frame 6, the range of FWHM widths of the filaments has climbed to 265-340  $\mu\text{m}$ ; the filaments are broadening and the spaces between filaments are beginning to emit appreciably. Finally, at late times (Fig. 3, top), the discrete filaments are no longer apparently distinct within the quasi-uniform emitting distribution.

The breakdown evolution process observed in experiments does not correspond with the structures predicted by magnetohydrodynamic (MHD) simulations based on the electric field magnitude in the target. In ALEGRA<sup>13,14</sup> simulations (Fig. 4), the electric field morphology is organized such that the peaks in field magnitude align with the helical gaps in the target (which are buried within the epoxy encapsulant). If, as was previously thought, the breakdown process in AutoMag liners depended directly on the magnitude and spatial distribution of the induced electric field, one would expect the breakdown to initiate and form helically oriented emitting structures. This is not what is observed; instead, discrete, primarily axially oriented emitting filaments (with respect to the axis of the cylindrical liner) tend to form in the manner previously described and illustrated in Fig. 3. The dynamic emission distributions observed in breakdown/flashover evolution in conjunction with these MHD simulation results indicate that the  $E_{gap}$  hypothesis does not accurately explain the propensity of AutoMag targets to undergo dielectric breakdown.

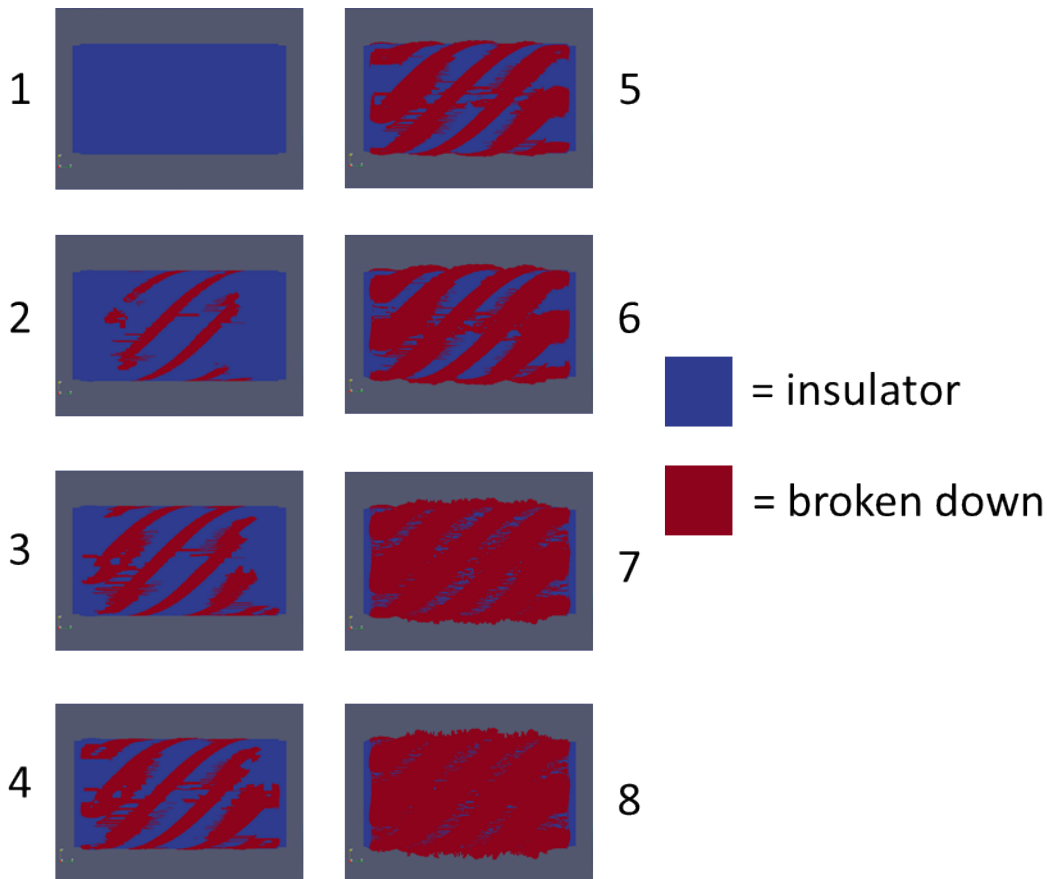


FIG. 4. – MHD modeling results from 3D ALEGRA. The outer surface of the target was modeled such that when an electric field magnitude threshold was surpassed, the material cells at the outer liner surface would go from a normal, insulating state (blue) to a conductive state (red). This enabled a preliminary (but incorrect) assessment of how electric field strength and topology was anticipated to affect breakdown initiation and evolution. Note how the post-breakdown material (red) is oriented in a helical sense corresponding with the helical gaps between metallic helices buried beneath the insulating material in the target, unlike the emission distributions in Fig. 2.

Additional experiments were designed to directly evaluate the primary working hypothesis of how flashover is initiated in AutoMag liners: namely that the magnitude of  $E_{gap}$  is the dominant mechanism driving flashover initiation. Previous experiments<sup>8</sup> indicated a value of  $E_{gap}$  in the range of 15-19 MV/m at the time of flashover initiation for epoxy-encapsulated targets which had 12.5° pitch angle helices; these targets were the only targets for which flashover occurred in previous 500-600 kA peak current experiments on Mykonos. Targets with larger pitch angle helices (20°, 30°, and 45°) that were pulsed with 500-600 kA in ~100 ns did not undergo breakdown.

Transient magnetic simulations in ANSYS Maxwell<sup>15</sup> suggested that a ~2X increase in  $E_{gap}$  can be accomplished by reducing the helical gap width by ~2X for AutoMag targets with 20° helices; such an increase in  $E_{gap}$  was hypothesized to cause flashover initiation at ~2X lower  $di/dt$ , i.e., earlier in the current pulse, for a target with the ~2X reduced gap width. Diagnostics were configured to capture this predicted, >20-ns difference in flashover initiation between nominal (500- $\mu$ m gap width) targets and targets with >2X thinner helical gaps. Targets with 200- $\mu$ m gaps and 20° helices were designed and manufactured for these experiments. Simulations indicate that decreasing the width of the helical gaps in the liner to 200  $\mu$ m while keeping the pitch angle, number of helical cuts, and spacing of helical cuts unchanged will result in significant increase of  $E_{gap}$  (>2X) with only a modest decrease (<10%) in  $B_{z,in}$ . Given that AutoMag liners have repeatedly demonstrated  $B_{z,in}$  in the 60-90 T range on Mykonos and that multiple measurements of  $B_{z,in}$  above 100 T were captured in Z experiments, the anticipated decrease in peak axial magnetic field is acceptable.

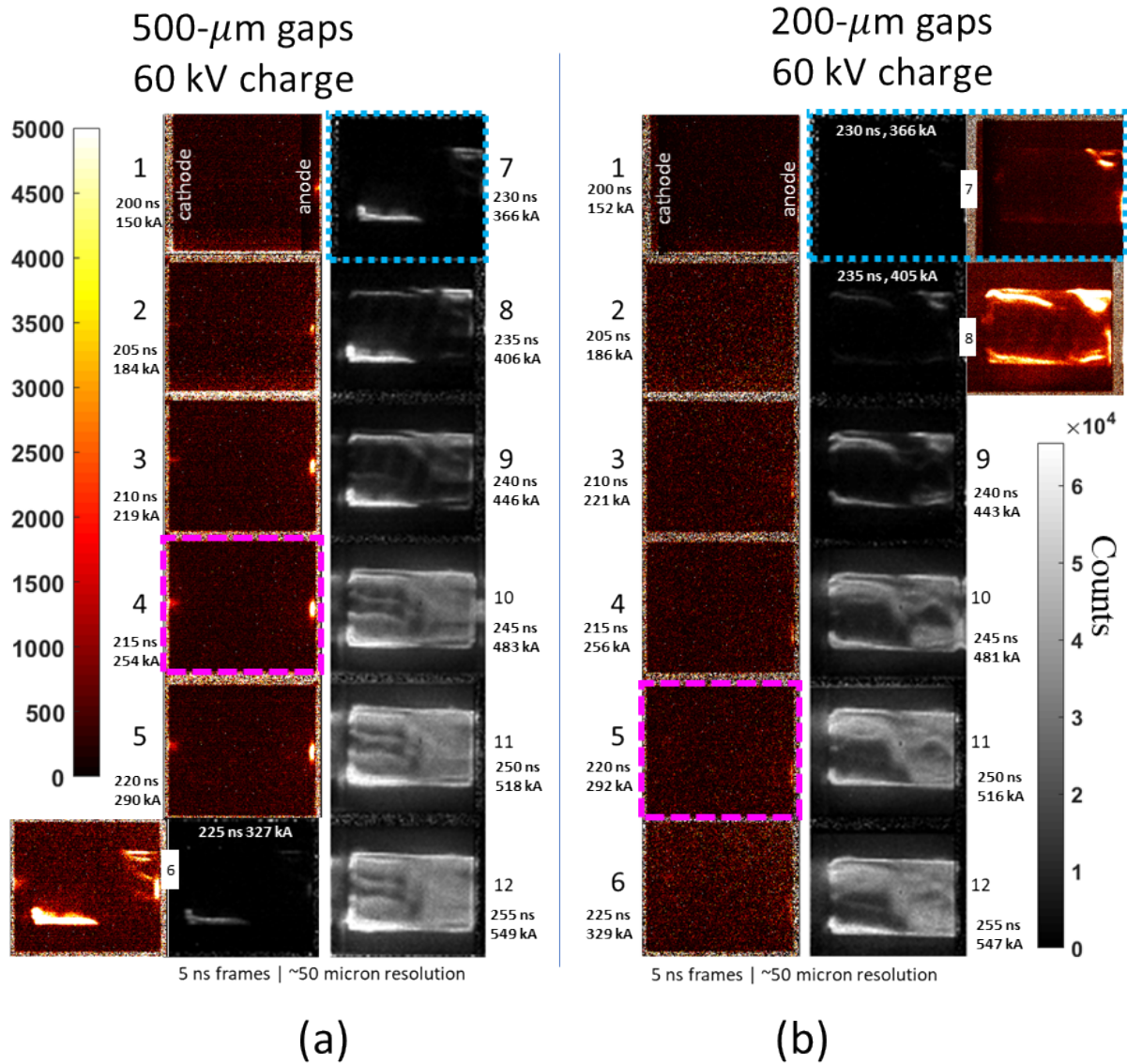


FIG. 5. – (a) 12-frame imaging data of an AutoMag experiment on Mykonos that used a target with 500- $\mu\text{m}$  wide, 20 $^\circ$  helical gaps that was pulsed with a  $\sim 650$  kA peak current pulse (60 kV charge voltage). (b) 12-frame imaging data taken at the same time(s) with respect to the current pulse as the data shown in (a) for an experiment using a target with 200- $\mu\text{m}$  wide, 20 $^\circ$  helical gaps what was pulsed with a  $\sim 650$  kA peak current pulse (60 kV charge voltage). Note the similarity in breakdown evolution in terms of timing and structure. The data in (b) indicate breakdown initiation that starts  $\sim 10$  ns (two frames) later than in (a). Frame 6 in (a) and frames 7 and 8 in (b) are shown with both transmission scales side by side to highlight the difference in emission characteristics between the earliest filaments and the late-time plasma distribution. The timing differences between the two experiments due to jitter of the pulsed power accelerator have been subtracted out and the data have been time shifted such that the frames in (a) and (b) are coincident with respect to the current pulses within  $\pm 1$  ns. The location of the cathode and anode are indicated in frame 1 of each dataset. Light blue dotted boxes indicate the frames during which breakdown initiation was inferred from APD data and magenta dashed boxes indicate the frame during which breakdown initiation was inferred from microBdot data.

The results of the 200- $\mu\text{m}$  gap experiments confirm that the  $E_{gap}$  breakdown hypothesis does not accurately describe the breakdown mechanism of AutoMag targets. The anticipated  $>20$  ns difference in breakdown initiation time between targets with 200- $\mu\text{m}$  gaps and targets with 500- $\mu\text{m}$  gaps (driven by current pulses with peak current within 3%) was not observed (Fig. 5 and Fig. 6); instead,

breakdown emission observed for the two types of target initiated within 5 ns of each other. In fact, the 200- $\mu\text{m}$  gap target that was predicted to breakdown  $>20$  ns earlier underwent breakdown initiation 1-5 ns **later** than the 500- $\mu\text{m}$  gap targets according to avalanche diode and microBdot probe data. The avalanche diode captured emission from breakdown initiation at 227 ns and 228 ns for the 500- $\mu\text{m}$  gap target and 200- $\mu\text{m}$  gap target experiments, respectively. The breakdown initiation times inferred from microBdot probe data (indicated by the departure of linear scaling of  $B_{z,in}$  with  $I(t)$ ) were 214 ns and 219 ns for the 500- $\mu\text{m}$  gap target and 200- $\mu\text{m}$  gap target experiments, respectively. These reported times and the times listed in Fig. 5 were shifted to remove timing jitter by matching the “half peak current” time,  $t_{half}$ , for each experiment (i.e.,  $I(t_{half}) = 0.5 * I_{peak}$ , where  $I_{peak} = \max(I(t))$ ).

Notably, the similarity of the breakdown time indicated by the avalanche diode (only a 1 ns difference) contrasts with the difference in breakdown initiation time inferred from microBdot probe data (a 5 ns difference). This indicates either that the field production mechanism in AutoMag targets begins to change due to current reorientation in the target prior to photoemission from the target or that the field of view of the avalanche diode may not have captured the earliest emission, perhaps due to the nonuniform azimuthal distribution of emitting filaments on the outer surface in conjunction with the field of view of the avalanche diode being limited to one side of the target. To discriminate between these possibilities, we consider other 60 kV charge voltage and 80 kV charge voltage experiments. Once again time shifting to match  $t_{half}$  for all datasets, breakdown initiation times indicated by the avalanche diode data and microBdot probe data are shown in Table I. Given the wide range of differences between  $t_{break}$  inferred from the avalanche diode data and from the microBdot probe data (1-15 ns, Table I), definitively determining the source of discrepancy is difficult. However, the observed ranges may be stronger support for the possibility that emission can initiate on the opposite side from the field of view of the diode, resulting in an apparent delay between the  $t_{break}$  data signature in the diode data compared to the microBdot probe data.

$V_{charge}$	Shot #	$t_{break}$ inferred from APD [ns]	$t_{break}$ inferred from microBdot [ns]
60 kV	10270	228	218
60 kV	10970	216	215
60 kV	10969	219	215
60 kV	10272	227	214
80 kV	10267	208	202
80 kV	10281	224	214
80 kV	10282	220	205

Table I. – Breakdown initiation times inferred from various AutoMag experiments during which both avalanche diode data and microBdot probe data were captured. These times have been time shifted to account for pulsed power machine jitter by shifting all datasets to match the time that the current is at half the peak value. Experiments that used 200- $\mu\text{m}$  gap targets are highlighted in green while unhighlights sections correspond to experiments that used 500- $\mu\text{m}$  gap targets.

The results of the 500- $\mu\text{m}$  gap target and 200- $\mu\text{m}$  gap target experiments indicate that the anticipated difference in  $E_{gap}$  did not result in a significant difference in breakdown timing. This surprising result motivated exploration of other paradigms for assessing breakdown initiation in AutoMag targets. Rather than calculating a local, average induced electric field within the helical gaps at the axial midplane, we investigated a calculated global induced electric field across the entire target and examined the induced electric field distribution in simulated AutoMag targets. Using experimental data, we then determine whether trends can best be explained in terms of these calculated and simulated parameters.

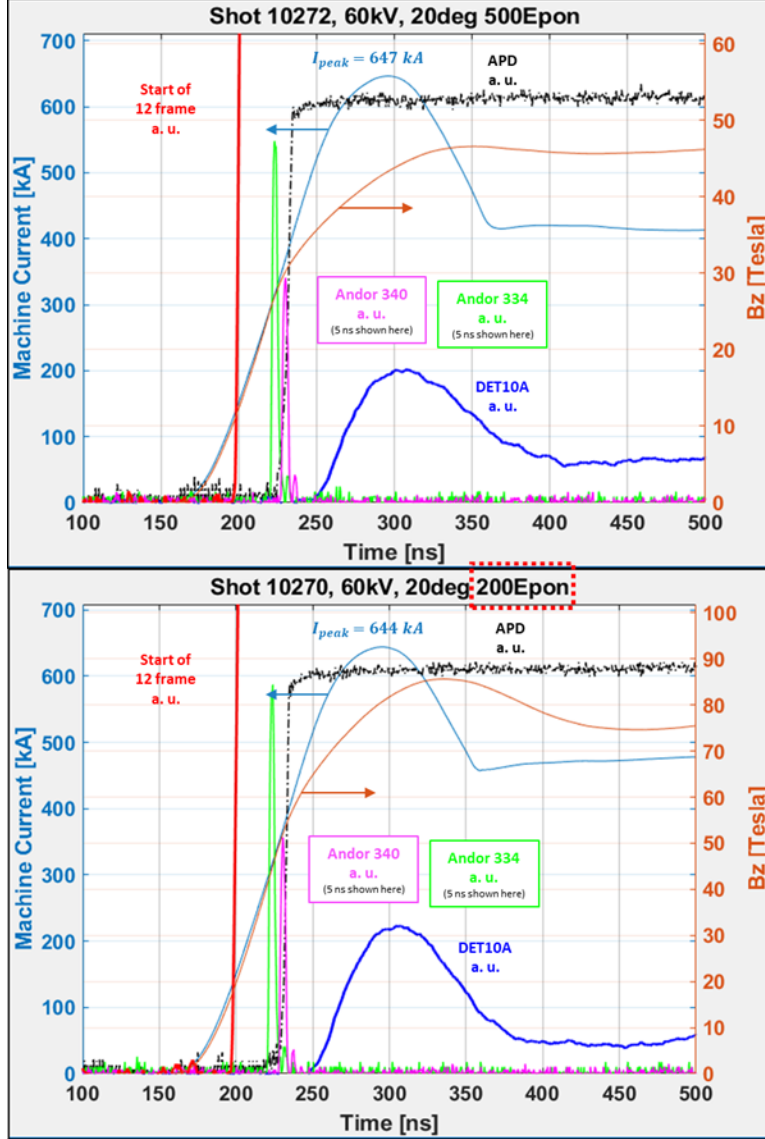


FIG. 6. – Plots of time-resolved data from the Mykonos experiments for which 12-frame data are shown in Fig. 5. The top plot corresponds to the data shown in Fig. 5(a) for an experiment utilizing a target with 500- $\mu\text{m}$  wide helical gaps and the bottom plot corresponds to the data shown in Fig. 5(b) for an experiment utilizing a target with 200- $\mu\text{m}$  wide helical gaps. The pink and green traces correspond to the frame monitor for two single-frame imagers, an Andor 340 and an Andor 334, that were fielded concurrently with the multi-frame imager.

The global average induced electric field across the axial length of the target,  $E_{global}$ , was calculated simply by multiplying the helical inductance,  $L_{helical}$ , of the AutoMag target by the current rise rate of the pulsed power driver at the time of breakdown,  $\left(\frac{dI}{dt}\right)_b$ , and dividing by the distance between the anode and cathode (the A-K gap distance, 12 mm) at the outer radius of the AutoMag target,  $l_{target}$ :

$$E_{global} = \frac{L_{helical} \left(\frac{dI}{dt}\right)_b}{l_{target}} \quad (1)$$

Here,  $L_{helical}$  is defined as the inductance of the target associated with the axial magnetic flux inside of the liner; the helical inductance excludes the inductance due to the (primarily) azimuthal magnetic

field generated outside of the liner. In other words, the helical inductance represents a lumped inductor circuit element at the end of the transmission line and the line inductance is the inductance of the entire transmission line up to the outer surface of the AutoMag target. As shown and discussed in Ref. 8, the internal axial magnetic flux is effectively switched out of the system when breakdown occurs as the current reorients to flow primarily axially on the outer (broken down) surface of the target rather than in the discrete metallic helices. Note that since the internal axial magnetic flux is switched out of the system after breakdown (i.e., the pulsed power driver circuit is no longer connected to the internal magnetic flux in the target), it subsequently decays on time scales associated with the resistance and inductance of decaying currents within the liner.

The global induced electric field can be thought of as a mechanism for switching current from a high inductance current path (current flowing within the metal helices) to a lower inductance current path (current flowing axially on the surface of the target after breakdown). In this sense, the propensity to undergo breakdown can be cast in terms of the difference in inductance between the pre-breakdown and post-breakdown states; a large difference would indicate that a target will be more likely to undergo breakdown at lower current rise rate whereas a smaller difference indicates that the inductive benefit of dielectric breakdown is small and the required current rise rate would need to be larger to initiate breakdown. The magnitude of  $E_{global}$ , or equivalently the magnitude of the inductive benefit to which we have referred, is what is postulated to drive the flashover process.

While  $E_{gap}$  was predicted to be  $\sim 2X$  higher in the 200- $\mu\text{m}$  gap targets, the calculated difference in helical inductance was  $<3\%$  ( $L_{helical,500gap} = 2.96 \text{ nH}$  vs.  $L_{helical,200gap} = 2.88 \text{ nH}$ ). For a current rise rate of 7.5 kA/ns (Fig. 1(d)),  $E_{global,500gap} = 1.85 \text{ MV/m}$  and  $E_{global,200gap} = 1.80 \text{ MV/m}$ . Framing the experimental results within the assumption of the  $E_{global}$  hypothesis, one would expect these two types of targets to undergo flashover/breakdown at very similar times at very similar current rise rates and this is indeed what was observed in experiments.

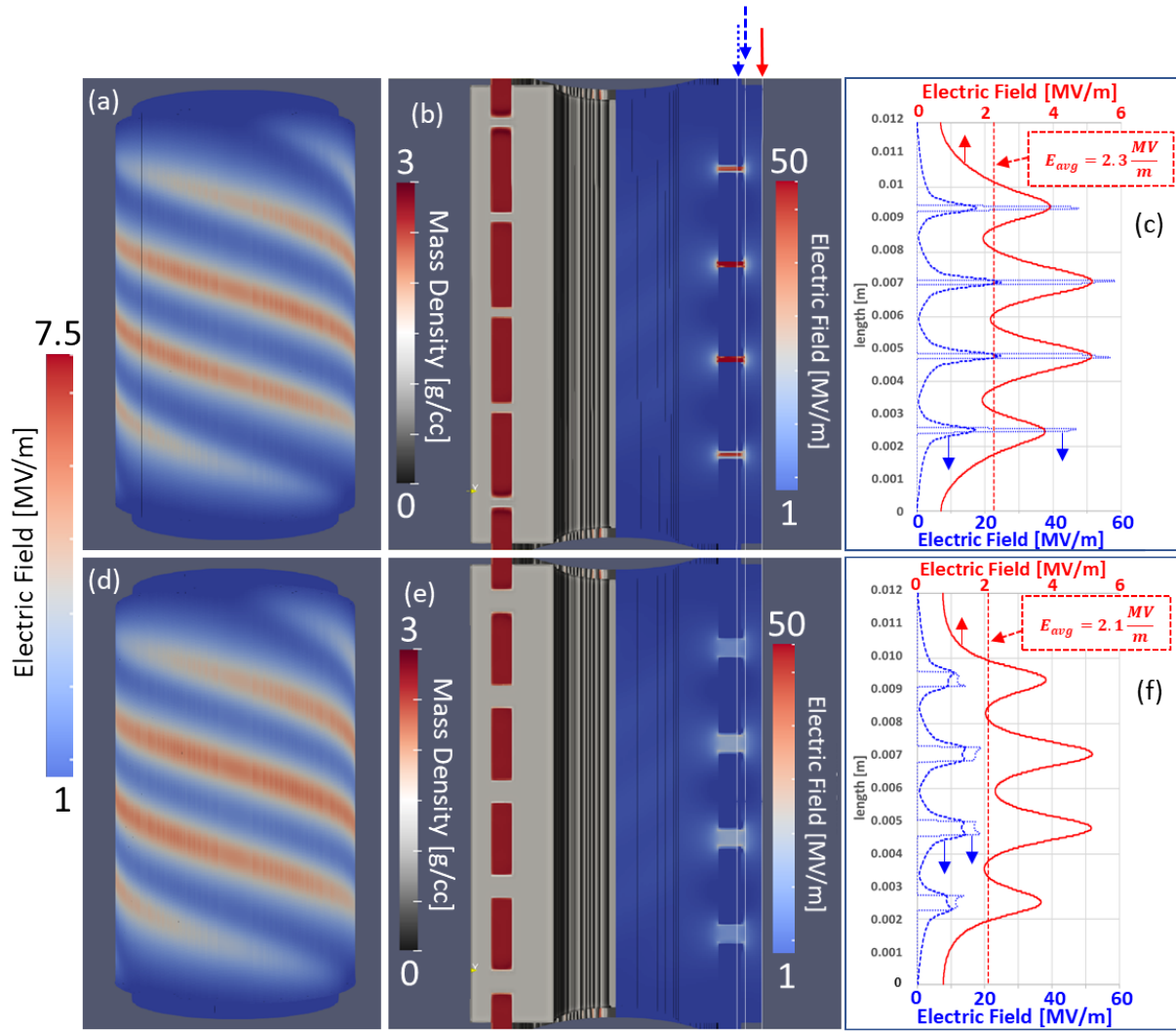


FIG. 7. – 3D ALEGRA simulation results. (a-c) show results from simulations of a 20° AutoMag target with 200- $\mu\text{m}$  wide helical gaps while (d-f) show results from simulations of a 20° AutoMag target with 500- $\mu\text{m}$  gaps. The simulation time,  $t = 223$  ns, for (a-c) corresponds to the current rise rate at which targets were observed to breakdown,  $dI/dt = 7.25$  kA/ns, during a  $\sim 650$  kA peak current pulse for 200- $\mu\text{m}$  gap experiments while the simulation time,  $t = 218$  ns, for (d-f) corresponds to the current rise rate at which targets were observed to breakdown,  $dI/dt = 7.27$  kA/ns, during a  $\sim 650$  kA peak current pulse for 500- $\mu\text{m}$  gap experiments. (a) and (d) are maps of electric field at the outer surface of the AutoMag targets. The corresponding colorbar for these two maps is located to the left. (b) and (e) are cross-section views of density maps on the left and electric field maps on the right. (c) and (f) show lineout plots of electric field along the lines indicated by the arrows above (b) and (e). The outermost lineout (solid red) at the outer insulator surface is tied to the top axis while the lineouts taken at the outer edge of the helical gaps (dashed blue) and 100  $\mu\text{m}$  inside of the helical gaps (dotted blue) are tied to the bottom axis. Note that the electric field inside of the gaps is much larger for the 200- $\mu\text{m}$  gap target, but for the lineout taken adjacent to the outer surface of the target (solid red), the electric field is comparable for the two targets. The averages taken for each of the outer surface lineouts (dashed red) is within 10% of each other: 2.1 and 2.3 MV/m for the 500- $\mu\text{m}$  gap and 200- $\mu\text{m}$  gap target simulations, respectively.

Simulations in the 3D MHD code ALEGRA were executed to explore the induced electric field distribution in both the 200- $\mu\text{m}$  gap and 500- $\mu\text{m}$  gap targets driven by as-measured Mykonos current pulses (Fig. 7). These simulations revealed that while peaks in electric field were evident locally in and around the individual helical gaps, the average field at the outer surface of the insulator was very similar (within 10%, Fig. 7(c) and 7(f)). Given that the emitting structures observed in imaging data appear to originate from the outer insulator surface, it is reasonable to think that the field

distribution on this surface influences breakdown initiation and dynamics. The simulation output time compared for each target type in Fig. 7 was chosen based on the measured  $dI/dt$  at which breakdown/flashover was observed in experiments; 7.3 kA/ns. This  $dI/dt$  value corresponds to  $E_{global,200gap,sim} = 1.7$  MV/m and  $E_{global,500gap,sim} = 1.8$  MV/m. Although the simulated electric field distribution (Fig. 7) is oriented such that the peaks in field align with the individual helical gaps, axially averaging the entire field distribution at the outer surface results in values of average electric field within 10% of each other:  $E_{avg,200gap} = 2.3$  MV/m and  $E_{avg,500gap} = 2.1$  MV/m (Fig. 7(c) and 7(f)).

The calculated  $E_{global}$  and simulated  $E_{avg}$  for these two targets do not correspond closely (20-30% difference between calculated  $E_{global}$  and simulated  $E_{avg}$  for a given target design). However, the similarity in  $t_{break}$  between the 200- $\mu$ m gap and 500- $\mu$ m gap targets corresponds with the <5% difference between  $E_{global}(t_{break})$  and the <10% difference in  $E_{avg}(t_{break})$ . This indicates that the induced electric fields at the outer surface of the target more heavily influence breakdown initiation compared to  $E_{gap}$  which is 2X larger in the 200- $\mu$ m gap target.

These experiments as well as those executed previously<sup>8</sup> indicate that enhancing the induced electric field in or around AutoMag liners during the current pulse (either by modifying the pitch angle of the helices or the driver  $dI/dt$ ) will enable earlier breakdown of the liner. As mentioned, decreasing the helical gap size does not result in the desired earlier breakdown; the close alignment of 200- $\mu$ m gap experiments and 500- $\mu$ m gap experiments instead indicates that the electric fields outside of the target, specifically at the outer surface of the insulator, influence breakdown initiation. This suggests that the most effective way to modify breakdown initiation is modification of the driver current pulse, enabling access to higher current rise rates (thus, higher  $E_{global}$  and/or  $E_{avg}$ ) earlier in the pulse (when internal field is lower, ideally in the 30-50 T range most relevant to MagLIF).

### III. Use of a pulsed UV laser to affect breakdown initiation

A UV laser could potentially be used to photoionize the outer layers of the insulator material in AutoMag liners, thereby providing a conductive plasma layer in which current can flow and trigger further breakdown of the insulator material. iCCD images of bulk insulated liners from previous Mykonos experiments<sup>8</sup> suggest that such a plasma distribution forms on the outer surface of the insulator after breakdown, but triggering the development of a plasma layer instead of relying on a surface flashover to occur with some degree of stochasticity would be extremely beneficial. Such a “triggered flashover” would enable greater control over the timing of current reorientation and cessation of internal axial magnetic field production. Thus the axial field inside of the liner could be more precisely controlled.

Previous work<sup>16</sup> suggests that a UV laser can be used to irradiate an insulator surface held at high electric field to initiate dielectric breakdown. There are notable differences between this previous work and the current work: (1) Enloe and Gilgenbach in Ref. 16 report on irradiating a rectangular surface compared to the cylindrical surface of the insulator in AutoMag targets; (2) the electrodes in the Ref. 16 experiments were held at static potential whereas the AutoMag target is being pulsed with current and thus subjected to a pulsed, inductive voltage; (3) the electrodes in Ref. 16 were completely electrically isolated with an insulator between them to serve as a current channel once broken down by the laser, but AutoMag targets initially are composed of a high inductance current

path (the helical conductors) and then develop a lower inductance current path in parallel once breakdown has occurred in the target.

AutoMag experiments utilizing a UV laser to promote surface breakdown were intended to reproduce the cited required laser fluence to affect breakdown initiation in Ref. 16: 5 – 65 mJ/cm<sup>2</sup>. To approximately reproduce the spectrum and fluence, an 80 mJ, 266-nm wavelength, 170 ps EKSPLA laser was used in AutoMag experiments. Several methods of irradiating the cylindrical outer surface of the target were explored. (1) The laser beam was split into three circular beams to irradiate 360° of the liner surface albeit with some degree of nonuniformity due to overlap of the beams. Splitting the beam three ways was accomplished with a 30/70 beam splitter followed by a 50/50 beam splitter (i.e., laser energy was split into three beams with 30%, 35%, and 35% of the total laser energy, respectively, not accounting for scattering or transmission losses). (2) A single unsplit circular beam was focused onto one side of the target to enable greater laser fluence. (3) A single unsplit beam was focused down to a 7-mm long, 1-mm wide line using a cylindrical lens (to further increase the fluence) which then irradiated one side of the liner. The laser used in Ref. 16 had a 60-ns pulse width whereas the EKSPLA laser used in this study has a 170-ps pulse width. However, it is stated in Ref. 16 that the power density of the laser did not seem to affect the breakdown characteristics of their experiments. Instead, the fluence of the beam was the most important factor. Given that assumption, 80 mJ of laser energy was thought to be sufficient to access the 5 – 65 mJ/cm<sup>2</sup> cited fluence range and was hypothesized to initiate breakdown in AutoMag targets.

Timing of laser irradiation of the target was configured to coincide with the peak  $dI/dt$  of the driver current pulse from Mykonos for all 45° liner experiments. Note that the 45° AutoMag liners have never been observed to undergo breakdown on Mykonos and are not expected to breakdown due solely to induced electric fields in the target. Peak  $dI/dt$  was selected to maximize the induced electric field in the target and thus maximize the likelihood of observing the effects of the laser on breakdown.

Implementing the first two laser configurations (three circular beams and one circular beam on target), did not result in any significant effect on breakdown dynamics in 45° targets. The beam energy was monitored during experiments with a laser energy meter; the beam was split using UV fused silica glass which sampled a small fraction of the total beam. The split in energy was characterized during benchtop tests prior to the Mykonos experiments; additionally, measurements were taken with the energy meter inside of the target chamber to account for all losses due to reflection and transmission through various elements in the optical path. As such, this measurement indicates the on-target laser energy. Unfortunately, large variations in the shot-to-shot laser energy existed, with the beam energy on target range of 12.5-32.0 mJ. For one unsplit circular beam with beam spot radius  $r_{spot} = 0.475$  cm, this constitutes a laser fluence of 17.7-45.2 mJ/cm<sup>2</sup>. Splitting the beam into three approximately equal beams reduces this fluence by a factor of approximately three (5.9 – 15.1 mJ/cm<sup>2</sup>), not accounting for overlaps in individual beams on target. While these fluence ranges fall within the cited range suggested by Ref. 16, no effect on breakdown was observed in the three-circular-beam and unsplit single-circular-beam experiments.

The failure of the laser to diagnosably affect breakdown initiation in experiments with three circular beams and a single unsplit circular beam on 45° targets prompted two changes to subsequent experiments. First, we elected to use AutoMag targets with 20° helices which undergo breakdown repeatably for 650-850 kA peak current pulses without laser irradiation. Instead of trying to initiate breakdown in targets in which it was not expected due to induced electric field (i.e., 45° liners), the focus shifted to using the laser to affect the timing of the initiation of the breakdown/flashover processes in targets that were expected to breakdown due to induced field at some point in the

current pulse (i.e., 20° targets). Second, we sought to access higher levels of laser fluence to more effectively photoionize a section of the outer liner surface and affect the flashover process. To accomplish this, the circular laser beam was focused down to a <1-mm wide, ~7-mm long line. This corresponds to a laser fluence range of 178.5 – 457.1 mJ/cm<sup>2</sup>, well above the range cited in Ref. 16. The given dimensions are estimates since the measurement of the beam relies on observation of fluorescence from a witness plate or piece of paper, which is accompanied by associated uncertainty and estimation.

For 45° targets, the laser line beam produced a narrow emitting distribution of plasma on the insulator surface that subsequently spread from the cathode side of the target (where the beam was pointed) towards the point at which the target contacts the anode (Fig. 8). Despite the apparent connection of emitting plasma between the cathode and anode, the multi-frame imaging data confirm that the emitting plasma remains localized to a thin line along one side of the target and flashover of the rest of the outer insulator surface did not occur. Diode and magnetic field data support that full, global flashover of the target and current reorientation did not occur. Specifically, diode data indicate emission that is far dimmer than that observed in experiments that underwent breakdown, indicating emission data that are similar to non-breakdown experiments. Magnetic field measured by microBdots maintained linear scaling with the drive current throughout the experiment, further indicating that full, global breakdown did not occur.

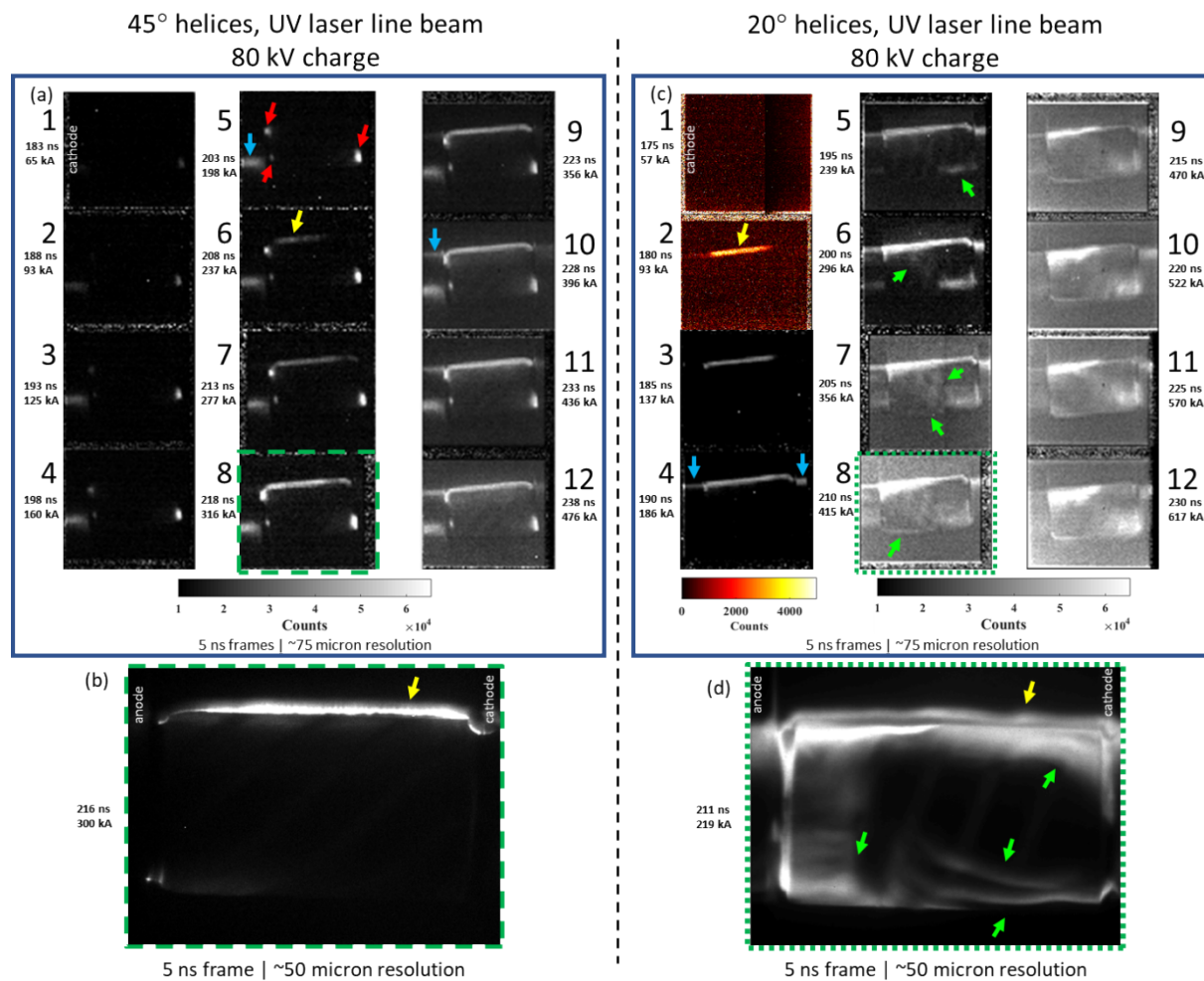


FIG. 8. – (a) 12-frame imaging data from a 45° AutoMag liner experiment on Mykonos that employed a pulsed UV laser focused down to a narrow line beam to impinge one side of the target (the top side as shown in figure). Yellow arrows indicate where the laser impinges on the liner, resulting in visible emission. Blue arrows indicate reflections off of hardware in the target region. Red arrows indicate photoemission associated with electrode contacts. In (a), note that the data show no signs of photoemission associated with additional discrete plasma filaments such as those observed in experiments that show full breakdown, only the single line of emission from the laser irradiating the target on one side of the target. (b) is an image from the same experiment as (a) taken using a single frame iCCD gated imager with a 5-ns gate width and filtered identically to the 12-frame imager. (c) shows 12-frame imaging data from a 20° AutoMag liner experiment on Mykonos which demonstrated transition from the single laser-induced line of emission towards formation of discrete emitting filaments and then a quasi-uniform emitting distribution similar to that observed in other non-laser experiments in which breakdown occurs. Green arrows indicate discrete plasma filaments that form as a result of breakdown/flashover. (d) An image from the same experiment as (c) taken using a single frame iCCD gated imager with a 5-ns gate width (with timing corresponding to frame 9 of the 12-frame data) and filtered identically to the 12-frame imager. The colorbar scale (data range) for frames 1 and 2 of (c) is a reduced range with a smaller maximum to indicate the relatively dim emission captured when the laser first irradiates the target in frame 2.

20° targets were used with UV laser line beam irradiation to test whether increasing the global induced electric field across the target combined with UV laser irradiation would result in flashover. Since breakdown was expected for 20° targets near peak  $dI/dt$  based on previous, non-laser Mykonos experimental data, timing of laser irradiation was shifted to be near half of peak  $dI/dt$ , >20 ns prior to when breakdown was observed in non-laser experiments. When 20° targets were irradiated with a UV laser line-focused-beam, multi-frame imaging confirms initial formation of a narrow emission distribution similar to 45° target experiments, but flashover of the target proceeds as multiple

discrete filaments of emitting plasma form and eventually merge together; this merging of individual filaments into a quasi-uniform emitting distribution is qualitatively consistent with non-laser 20° target experiments driven by 650-850 kA peak current pulses on Mykonos, though some important differences are apparent.

Similar to non-laser experiments, in laser-driven experiments discrete filaments form on the surface of the 20° target and eventually the entire outer surface forms a photoemitting distribution (frame 12, Fig. 8(c)). Interestingly, the line of emission from the irradiation of the laser (Fig. 8(c), frame 2) persists for three full frames (15 ns) before formation of another, separate filament is apparent (Fig. 8(c), frame 5, green arrow). Additional filaments continue to appear (Fig. 8(c), frames 6-8) and then the regions between filaments begin to emit more brightly as time progresses (Fig. 8(c), frames 9-12). Unlike in previous 20° target experiments, multi-frame imaging data indicate that there are sections of the emitting surface that emit more brightly and continue to emit more brightly than neighboring sections of the target surface until the final frame. For example, the top left corner and bottom right corner of the target surface in Fig. 8(c), frame 12 are emitting 50-75% more brightly than the bottom left and top right corners on average. Compare this to the 20-30% variations in emission across the target surface that are apparent in non-laser imaging data such as that shown in frame 12 of Fig. 2(a), (b), and (c). This could indicate that a different plasma distribution is forming in 20° target experiments with UV laser irradiation with a line beam spot shape, perhaps a distribution with larger spatial nonuniformities in temperature and electrical conductivity. Whether this surface plasma evolves to a more uniform emitting distribution at later time (similar to what was observed in non-laser 20° target experiments) is unknown.

Analysis of magnetic field data indicates that the laser has a diagnosable effect on the timing of breakdown initiation (Fig. 9). By time shifting the data to match the rising edges of microBdot probe signal for laser and non-laser experiments, it becomes apparent that the timing of flashover initiation is significantly earlier for experiments employing the UV laser (Fig. 9); 20-30 ns earlier for 80 kV charge voltage experiments and 30-40 ns earlier for 60 kV charge voltage experiments. For 60 kV charge voltage experiments (Fig. 9(a)), the time that the laser irradiates the target occurs ~5 ns prior to deviation of the microBdot data from the other, non-laser microBdot datasets. For 80 kV charge voltage experiments, (Fig. 9(b)), the time that the laser irradiates the target occurs <3 ns prior to deviation of the microBdot data from non-laser microBdot datasets. The microBdot data from both 60 kV and 80 kV shots indicates that the laser effectively lowers the required  $dI/dt$  (and therefore, the  $E_{global}$  and/or  $E_{avg}$ ) at which flashover will initiate, indicating that the timing of flashover can indeed be affected by using a pulsed UV laser to irradiate the outer surface of an AutoMag target.

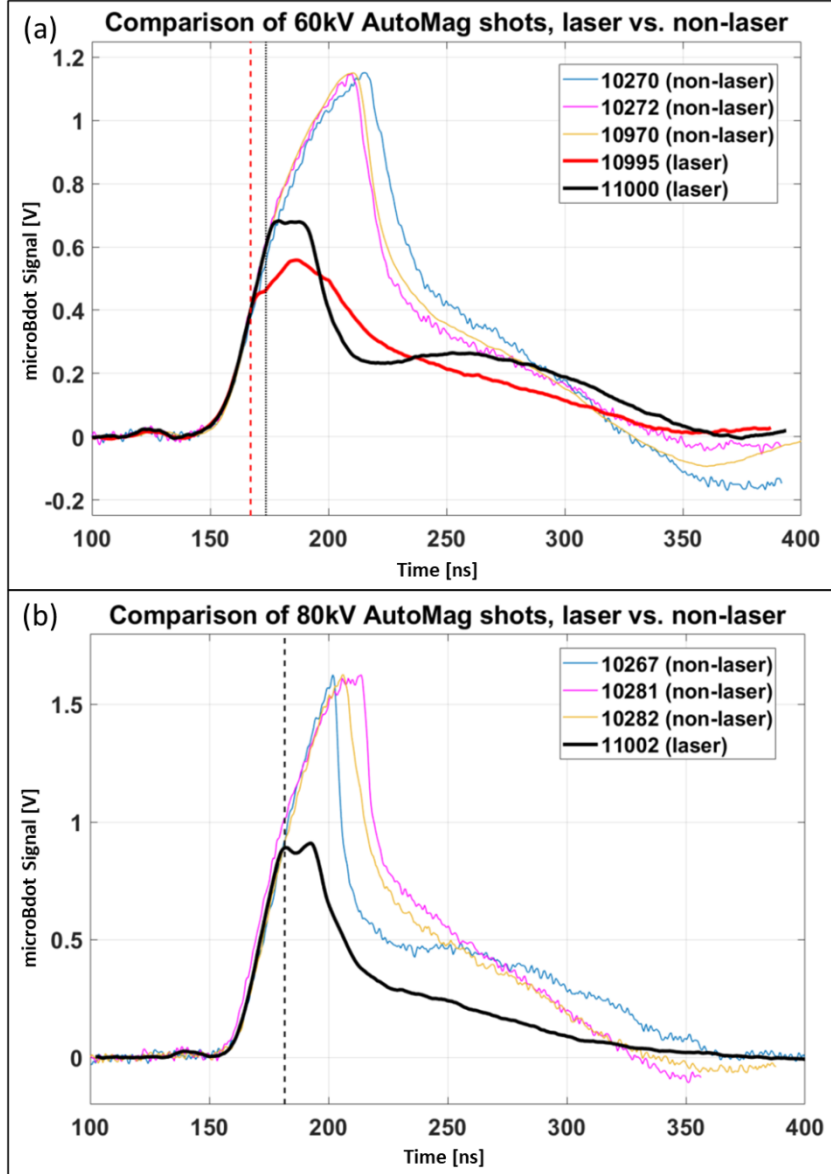


FIG. 9. – Plots of signal from microBdot probes. The signal is a measurement of the time derivative of axial magnetic field inside of the AutoMag liner,  $dB_{z,in}/dt$ , measured near the axial midplane. All data shown is for targets with  $20^\circ$  helices. Time for each dataset has been shifted to match up the rising edge of each signal. (a) Data from three 60 kV charge voltage experiments in which a UV laser was not used (and the target underwent flashover due to induced electric fields in the target) are shown from shots 10270 (blue), 10272 (magenta), and 10970 (yellow) in thin color. Data for non-laser experiments have been normalized to match the peak signal value of shot 10270. Data for experiments in which a UV pulsed laser (focused down to a  $\sim 7$  mm  $\times$  1 mm beam) was used to irradiate the outer surface of the target are shown in bolded red for shot 10995 and bolded black for shot 11000. Signal amplitude for data from UV irradiated experiments has been normalized to match the rising edge of the non-laser experimental data. The vertical red dashed line indicates the time that the laser irradiated the outer surface of the liner in shot 10995 and the vertical black dotted line indicates the time that the laser irradiated the outer surface in shot 11000. (b) Data from three non-laser 80 kV charge voltage experiments are shown from shots 10267 (blue), 10281 (magenta), and 10282 (yellow) in thin color. Data for non-laser experiments have been normalized to match the peak signal value of shot 10267. Data for experiments in which a UV pulsed laser (focused down to a  $\sim 7$  mm  $\times$  1 mm beam) was used to irradiate the outer surface of the target are shown in bolded black for shot 11002. Data for UV irradiated experiments has been normalized to match the rising edge of the non-laser experimental data for this plot. The vertical black dashed line indicates the time that the laser irradiated the outer surface in shot 11002.

#### IV. Summary of breakdown experiment results

Comparing  $E_{global}$  across the numerous AutoMag experiments executed to date provides an opportunity to evaluate how well  $E_{global}$  functions as a metric for assessing breakdown propensity in AutoMag targets. Just as simulated  $E_{avg}$  was compared for 500- $\mu\text{m}$  and 200- $\mu\text{m}$  gap targets in Fig. 7,  $E_{global}$  can be compared across the different target types (12.5°, 20°, 45° helices with 200- $\mu\text{m}$  or 500- $\mu\text{m}$  gaps) and different driver current pulses (500 – 850 kA peak current Mykonos pulses and ~20 MA peak current shaped pulses on the Z accelerator). Using the inferred time of breakdown from microBdot data for AutoMag experiments across these different target and driver configurations,  $E_{global}$  values were calculated and are compared in Fig. 10.

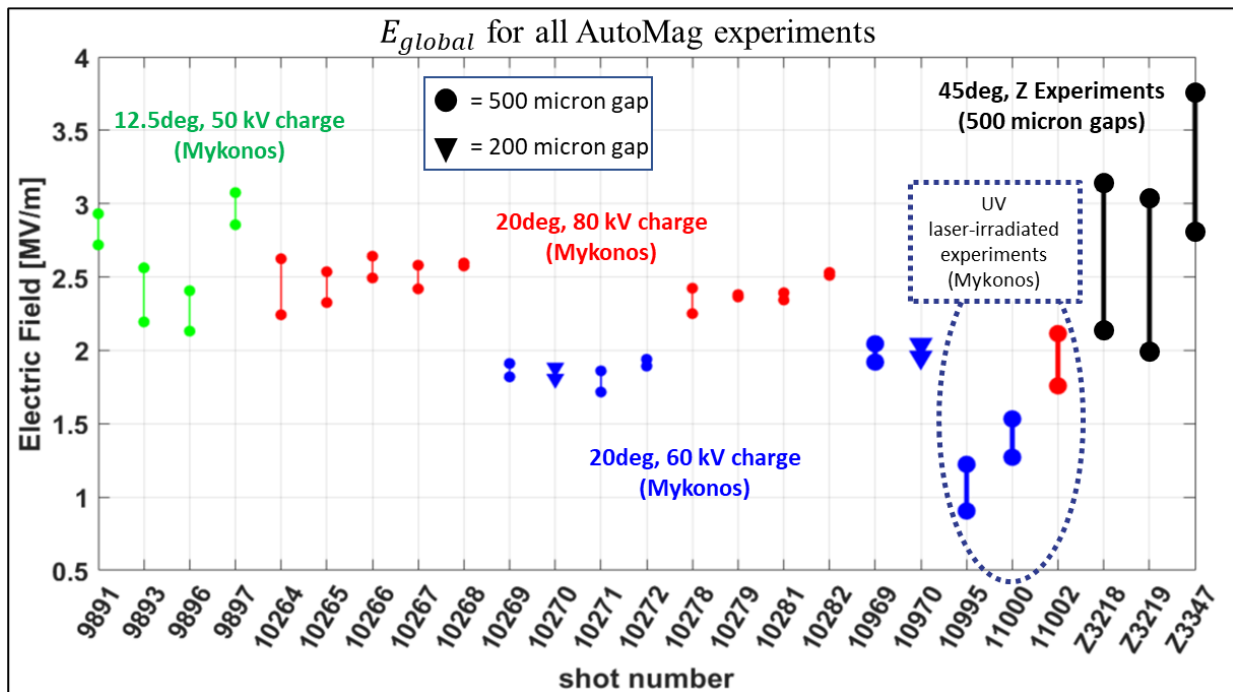


FIG. 10. – Plot of all AutoMag experiments in which dielectric breakdown was observed with optical diagnostics and inferred from electrical diagnostics (microBdots and/or driver current monitors). The range bars for each shot are assigned based on a time uncertainty of +/- 5 ns for the non-laser Mykonos experiments and +/- 2.5 ns for the Mykonos experiments that used the UV laser and for the Z experiments. The central value for this uncertainty range corresponds to the point of divergence between the microBdot data and the load current monitor data for both Mykonos and Z experiments shown.

$E_{global}$  was lower for the three laser-irradiated AutoMag shots on Mykonos (Fig. 10) compared to the non-laser shots with same target and driver configuration, suggesting a measurable effect that the laser had on breakdown initiation in the experiments. Comparison of  $E_{global}$  for all of the non-laser AutoMag experiments shown in Fig. 10 indicates a range from approximately 1.9 – 3.75 MV/m. Interestingly, the average  $E_{global}$  for certain target types and driver configurations aligns more closely; 20°, 80 kV charge shots on Mykonos (Fig. 10 shown in red) all appeared to initiate breakdown at  $E_{global} = 2.4 \pm 0.25$  MV/m whereas 20°, 60 kV charge shots on Mykonos (Fig. 10 shown in blue) all appeared to initiate breakdown at  $E_{global} = 1.9 \pm 0.2$  MV/m. Recall that MHD simulations in ALEGRA of 200- $\mu\text{m}$  gap and 500- $\mu\text{m}$  gap targets (Fig. 7) indicated that the  $E_{avg}$  at the outer insulating surface was 2.1 MV/m and 2.3 MV/m, respectively, which compares favorably with the observed ranges of  $E_{global}$  for 20°, 80 kV and 20°, 60 kV shots regardless of gap size. 12.5°, 50 kV charge shots

on Mykonos were observed to breakdown in a range of  $E_{global} = 2.25 - 3$  MV/m. The range of  $E_{global} = 2.0 - 3.75$  MV/m for Z experiments, though an admittedly wide range, can be compared with the ranges of  $E_{global}$  calculated from the numerous Mykonos experiments. Notably the uncertainty in the calculated  $E_{global}$  is larger for the Z experiments (owing primarily to the much more quickly varying  $dI/dt$  values associated with Z compared to Mykonos).

## V. Study of novel encapsulant insulating material to improve initial mass density uniformity

The nonuniform density distribution in AutoMag liners is a non-ideal element of the target concept from the standpoint of implosion symmetry. Previous inertial confinement fusion target designs have failed due to mass density nonuniformities which have tended to exacerbate development of deleterious implosion instabilities<sup>17</sup>. Similarly, the metallic and insulator-filled helices in AutoMag result in a nonuniform electrical conductivity distribution. The electrical conductivity distribution is much more integral to the concept while the mass density distribution can potentially be modified. The insulator material in AutoMag targets is formed from a flowable epoxy, so mixing in higher mass density material prior to solidification of the encapsulant can increase the average mass density of the insulating material.

Boron carbide powder ( $\rho_{B_4C} = 2.51$  g/cm<sup>3</sup>) was used to increase the average mass density of the cured encapsulant mixture. Boron carbide in solid form is an electrically semi-conductive material, but in powder form is thought to have very low electrical conductivity similar to aluminum oxide (alumina). The electrical conductivity of the mixture was not directly measured during this study and it was unclear how doping the epoxy would impact the dielectric breakdown process in AutoMag.

To explore this experimentally, AutoMag targets were manufactured with aluminum helices encapsulated by a 50/50 (mass percent) mixture of EPON and boron carbide powder. This mixture has a density of 1.81 g/cm<sup>3</sup> compared to beryllium solid density, 1.85 g/cm<sup>3</sup>. The resultant mixture is black and opaque to visible spectrum photons (unlike EPON which is translucent for visible spectrum photons). Targets with 20° helices were the primary focus of these doped insulator target studies since in previous experiments using regular EPON dielectric breakdown was regularly observed when pulsed with 650 – 850 kA on Mykonos.

In all experiments utilizing the boron-carbide-doped insulator mixture, optical diagnostics did not measure *any* photoemission from the outer surface of the target aside from the electrode contacts. Recall that photoemission had been repeatedly observed in non-doped insulator targets. Additional shots were executed in which optical density filtering was removed and the sensitivity of the time-resolved photosensitive diodes and optical imagers was increased; the single frame imager sensitivity increased by 20X, the 12-frame imager sensitivity increased by ~8X, and the diode sensitivities were increased by 100X. Even after increasing the sensitivity of optical diagnostics the emission either still remained below the threshold of detection or was entirely not present. Note that photoemission from the electrode contacts at either end of the liner was still observed by optical diagnostics, particularly the imagers, in both the low and high sensitivity configurations.

Axial magnetic field measured inside of doped insulator AutoMag experiments indicates that current reorientation of some kind occurred, but importantly, the point at which the internal magnetic field data and the driver current data cease linear scaling occurs much earlier in the current pulse (black arrow, Fig. 11). As well, the internal magnetic field data continues to rise significantly after the point

of divergence (Fig. 11). Though qualitatively similar continued rise in magnetic field data is apparent in other (non-doped-insulator) AutoMag data sets from Mykonos experiments, this post-divergence behavior suggests that field may have risen by a factor of  $\sim 10X$  and reached a maximum value after peak current of the accelerator. Once again, a post-peak current maximum in the internal axial magnetic field is not unprecedented, especially given that the breakdown is suspected to isolate the internal axial magnetic flux from the driver, implying that the internal axial field would decay away with a characteristic timescale different than the rise time or post-peak-current fall time of the driver current.

Magnetic field probe data and optical emission diagnostic data indicate that these doped-insulator experiments operate differently than normal AutoMag targets. Dielectric breakdown may be occurring in doped-insulator targets but is simply not observed by the optical diagnostics. This could be the case if the breakdown was occurring either on the inner surface of the target or locally near the helical gaps, buried beneath the surface of the insulator material. Since the doped-insulator mixture is optically opaque, both of these scenarios would result in lack of photon production that could be measured by the optical diagnostic suite. Data suggest that the electrical properties of the insulating medium are significantly changed by introducing the boron carbide powder dopant.

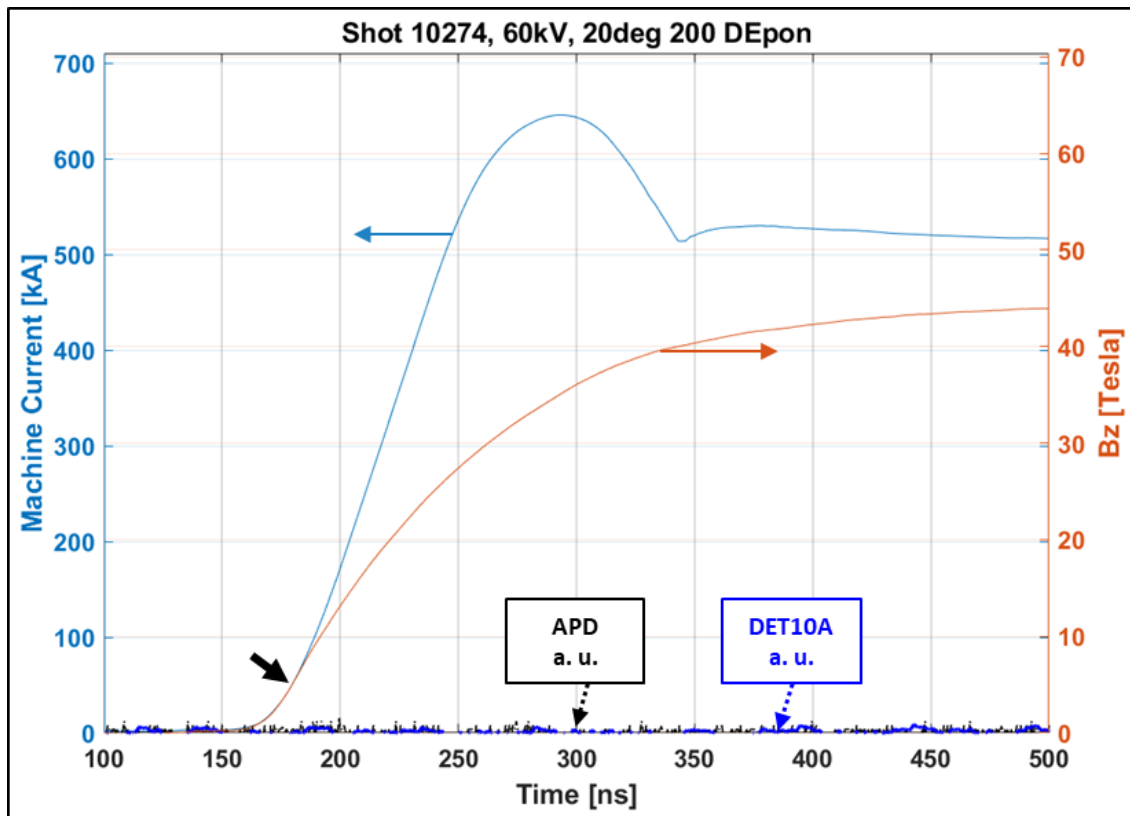


FIG. 11. – Plot of time-resolved data from a  $20^\circ$ ,  $200\text{-}\mu\text{m}$  wide helical gap AutoMag liner experiment that used boron-carbide-doped EPON for the insulating encapsulant material. The black arrow indicates the time at which the microBdot data and the driver current monitor data cease linear scaling, indicating breakdown. Note that this divergence occurs much earlier than in other AutoMag experiments that used undoped encapsulant (whether Stycast or EPON) and that were pulsed with a similar current pulse (see Fig. 6, bottom).

## VI. Conclusions and path forward

The first time-resolved imaging data have been captured for the dielectric breakdown process in AutoMag liners. This has enabled assessment of the timescale of the breakdown process as well as the time-dependent emission distribution dynamics of the observed post-breakdown surface plasma structures. By comparing time-resolved (multi-frame) imaging data with other time resolved diagnostics, namely microBdot probe data and avalanche diode data, the breakdown process has been analyzed and compared across numerous experiments on multiple pulsed power facilities (the 600-900 kA, ~100-ns rise time Mykonos accelerator and the ~20 MA, ~100-ns rise time Z accelerator). Transient magnetic simulations and MHD simulations have enabled further study of the magnetic and electric field distributions within AutoMag targets, providing comparisons to data and opportunities to develop hypotheses regarding the dominant factors driving breakdown timing and evolution. Rather than being dominated by the strength of the average induced electric field within the helical gaps as was previously thought, experiments reported in this article as well as simulations executed to compare to the reported experiments indicate that the electric field distribution at the outer insulating surface of the AutoMag liner likely is a larger influence on the breakdown process.

Use of a pulsed UV laser irradiating the outside surface of AutoMag targets was found to diagnosably affect the breakdown process for some AutoMag configurations. MicroBdot probe data indicate that internal field production is altered as a result of the UV laser irradiating the target; linear scaling between the measured internal magnetic field and the drive current, an indication of breakdown initiation, occurs 20-40 ns earlier than in non-laser experiments. Multi-frame imaging indicates similar post-breakdown emission distribution dynamics as non-laser experiments, although 30-40% larger nonuniformities in the photoemission distribution at the outside surface are apparent in multi-frame imaging data. While these experiments excitingly indicate a path towards using UV lasers to facilitate precise control of the breakdown process (and thus control of the magnitude of the uncompressed internal field), additional exploration and optimization is likely necessary before successful implementation in full scale magneto-inertial fusion AutoMag-MagLIF experiments.

A novel encapsulant material, EPON mixed with boron carbide powder, was explored to determine whether adding dopant material to the encapsulant would influence field production and breakdown. Experiments show that the mass doped encapsulant material undergoes breakdown in a significantly different manner compared to targets employing EPON alone. Measured internal magnetic field indicates much earlier breakdown for the mixed encapsulant but optical diagnostics indicate a complete absence of photoemission from the outside surface of the target.

## Acknowledgements

The authors would like to thank P. F. Schmit for carefully reviewing this manuscript and suggesting improvements. The authors gratefully acknowledge helpful discussions with S. A. Slutz, C. A. Jennings, C. Siefert, A. C. Robinson, E. P. Yu, D. C. Lamppa, R. D. McBride, M. A. Gilmore, E. Schamiloglu, G. R. Laity, D. J. Ampleford, T. M. Hutchinson, K. J. Peterson, K. Beckwith, G. A. Rochau, B. Jones, M. E. Cuneo, and D. B. Sinars. The authors would also like to thank J. Greenly for advice and consultation regarding miniature magnetic field probe fabrication and calibration and J. Moore and M. Savage for assistance with calibration of miniature magnetic field probes.

This work was partially funded by the National Nuclear Security Administration through the Krell Institute via the Stewardship Science Graduate Fellowship through Grant No. DE-NA0003864. This work was also funded in part by Sandia's Laboratory Directed Research and Development program via Project Nos. 195306 and 200269 and via the Truman Fellowship, Project No. 226067. Sandia National Laboratories is a multi-mission laboratory managed and operated by National Technology and Engineering Solutions of Sandia, LLC, a wholly owned subsidiary of Honeywell International, Inc., for the U.S. Department of Energy's National Nuclear Security Administration under Contract No. DE-NA-0003525. This paper describes objective technical results and analysis. Any subjective views or opinions that might be expressed in the paper do not necessarily represent the views of the U.S. Department of Energy or the United States Government.

<sup>1</sup> S. A. Slutz, M. C. Herrmann, R. A. Vesey, A. B. Sefkow, D. B. Sinars, D. C. Rovang, K. J. Peterson, and M. E. Cuneo, *Phys. Plasmas* 17, 056303 (2010).

<sup>2</sup> M. R. Gomez, S. A. Slutz, A. B. Sefkow, D. B. Sinars, K. D. Hahn, S. B. Hansen, E. C. Harding, P. F. Knapp, P. F. Schmit, C. A. Jennings, T. J. Awe, M. Geissel, D. C. Rovang, G. A. Chandler, G. W. Cooper, M. E. Cuneo, A. J. Harvey-Thompson, M. C. Herrmann, M. H. Hess, O. Johns, D. C. Lamppa, M. R. Martin, R. D. McBride, K. J. Peterson, J. L. Porter, G. K. Robertson, G. A. Rochau, C. L. Ruiz, M. E. Savage, I. C. Smith, W. A. Stygar, and R. A. Vesey. *Phys. Rev. Lett.* 113, 155003 (2014).

<sup>3</sup> M. K. Matzen, B. W. Atherton, M. E. Cuneo, G. L. Donovan, C. A. Hall, M. Herrmann, M. L. Kiefer, R. J. Leeper, G. T. Leifeste, F. W. Long, G. R. McKee, T. A. Mehlhorn, J. L. Porter, L. X. Schneider, K. W. Struve, W. A. Stygar, and E. A. Weinbrecht, *Acta Phys. Pol. A* 115, 956 (2009).

<sup>4</sup> D. V. Rose, D. R. Welch, E. A. Madrid, C. L. Miller, R. E. Clark, W. A. Stygar, M. E. Savage, G. A. Rochau, J. E. Bailey, T. J. Nash, M. E. Sceford, K. W. Struve, P. A. Corcoran, and B. A. Whitney, *Phys. Rev. Spec. Top. Accel. Beams* 13, 010402 (2010).

<sup>5</sup> D. C. Rovang, D. C. Lamppa, M. E. Cuneo, A. C. Owen, J. McKenney, D. W. Johnson, S. Radovich, R. J. Kaye, R. D. McBride, C. S. Alexander, T. J. Awe, S. A. Slutz, A. B. Sefkow, T. A. Hail, P. A. Jones, J. W. Argo, D. G. Dalton, G. K. Robertson, E. M. Waisman, D. B. Sinars, J. Meissner, M. Milhous, D. N. Nguyen, and C. H. Mielke, *Rev. Sci. Instrum.* 85, 124701 (2014).

<sup>6</sup> S. A. Slutz, C. A. Jennings, T. J. Awe, G. A. Shipley, B. T. Hutsel, and D. C. Lamppa, *Phys. Plasmas* 24, 012704 (2017).

<sup>7</sup> G. A. Shipley, T. J. Awe, B. T. Hutsel, J. B. Greenly, C. A. Jennings, and S. A. Slutz, *Physics of Plasmas* 26, 052705 (2019).

<sup>8</sup> G. A. Shipley, T. J. Awe, B. T. Hutsel, S. A. Slutz, D. C. Lamppa, J. B. Greenly, and T. M. Hutchinson, *Physics of Plasmas* 25, 052703 (2018).

<sup>9</sup> J. Greenly, M. Martin, I. Blesener, D. Chalenski, P. Knapp, and R. McBride, *AIP Conf. Proc.* 1088, 53 (2009).

<sup>10</sup> M. G. Mazarakis, W. E. Fowler, K. L. LeChien, F. W. Long, M. K. Matzen, D. H. McDaniel, R. G. McKee, C. L. Olson, J. L. Porter, S. T. Rogowski, K. W. Struve, W. A. Stygar, J. R. Woodworth, A. A. Kim, V. A. Sinebryukhov, R. M. Gilgenbach, M. R. Gomez, D. M. French, Y. Y. Lau, J. C. Zier, D. M. VanDevalde, R. A. Sharpe, and K. Ward, "High-current linear transformer driver development at Sandia National Laboratories," *IEEE Trans. Plasma Sci.* 38(4), 704–713 (2010).

<sup>11</sup> S. A. Slutz, M. R. Gomez, S. B. Hansen, E. C. Harding, B. T. Hutsel, P. F. Knapp, D. C. Lamppa, T. J. Awe, D. J. Ampleford, D. E. Bliss, G. A. Chandler, M. E. Cuneo, M. Geissel, M. E. Glinsky, A. J. Harvey-Thompson, M. H. Hess, C. A. Jennings, B. Jones, G. R. Laity, M. R. Martin, K. J. Peterson, J. L. Porter, P. K. Rambo, G. A. Rochau, C. L. Ruiz, M. E. Savage, J. Schwarz, P. F. Schmit, G. Shipley, D. B. Sinars, I. C. Smith, R. A. Vesey, and M. R. Weis, *Physics of Plasmas* 25, 112706 (2018)

<sup>12</sup> M. R. Gomez, J. C. Zier, R. M. Gilgenbach, D. M. French, W. Tang, and Y. Y. Lau, *Review of Scientific Instruments* 79, 093512 (2008).

<sup>13</sup> A. C. Robinson, T. A. Brunner, S. Carroll, R. Drake, C. J. Garasi, T. Gardiner, T. Hail, H. Hanshaw, D. Hensinger, D. Labreche, R. Lemke, E. Love, C. Luchini, S. Mosso, J. Niederhaus, C. C. Ober, S. Petney, W. J. Rider, G. Scovazzi, O. E. Strack, R. Summers, T. Trucano, V. G. Weirs, M. Wong, and T. Voth, *Proceedings of the 46<sup>th</sup> AIAA Aerospace Sciences Meeting*. AIAA-2008-1235.

<sup>14</sup> A. C. Robinson and C. J. Garasi, *Comput. Phys. Commun.* 164, 408 (2004).

<sup>15</sup> See <https://www.ansys.com/products/electronics/ansys-maxwell> for information regarding the Maxwell software package and its low-frequency transient magnetic solver.

<sup>16</sup> Enloe, C.L., Gilgenbach, R.M. *Ultraviolet-induced flashover of a plastic insulator using a pulsed excimer laser*. *Plasma Chem Plasma Process* 7, 89–99 (1987)

<sup>17</sup>D. D. Ryutov, M. S. Derzon, and M. K. Matzen, *Rev. Mod. Phys.* 72, 167 (2000).